· Article · Advances in Polar Science
doi:10.12429/j.advps.2025.0043 March 2026 Vol. 37 No. 1: 43-55

A multi-tie points-based method for retrieving of the Arctic thin sea ice thickness from SMOS

LI Jiaxing[1,2,3], ZHANG Shengkai[1,2,3,*], XIAO Feng[1,2,3], GENG Tong[1,2,3] & LI Fei[1,2,4]

[1] Chinese Antarctic Center of Surveying and Mapping, Wuhan University, Wuhan 430071, China;
[2] Key Laboratory of Polar Environment Monitoring and Public Governance, Ministry of Education, Wuhan 430079, China;
[3] School of Geodesy and Geomatics, Wuhan University, Wuhan 430079, China;
[4] Department of Earth and Space Sciences, Southern University of Science and Technology, Shenzhen 518055, China

Received 17 November 2025; accepted 19 January 2026; published online 30 March 2026

Abstract The correlation between the Soil Moisture and Ocean Salinity (SMOS) L-band brightness temperature and thin sea ice thickness has been widely exploited using semi-empirical retrieval approaches based on a single-tie point (STP). However, due to pronounced spatial heterogeneity in seawater and sea ice properties across the Arctic, the use of an STP often leads to regionally biased. To address this limitation, this study proposes a multi-tie point (MTP) sea ice thickness retrieval method based on SMOS brightness temperature and sea ice concentration time series. Multiple seawater and sea ice tie-point values are identified through point-by-point time series analysis, quality control, and statistical hypothesis testing, allowing spatial variability in radiometric properties to be explicitly considered. The MTP-based retrieval is applied to Arctic freeze-up conditions. Validation against independent SMOS thin sea ice thickness products shows that the MTP approach yields significantly reduced bias and root mean square error compared with the conventional STP method, with statistically significant improvements confirmed by paired *t*-tests. While retrieval accuracy stabilizes beyond a certain number of tie points, the preprocessing cost associated with tie-point selection increases substantially. Considering both accuracy and efficiency, the MTP framework provides a practical and robust approach for large-scale Arctic thin sea ice thickness retrieval and enables improved characterization of regional freezing processes and maximum ice thickness.

Keywords **SMOS**, **single-tie point**, **Arctic**, **multi-tie point**, **thin sea ice thickness**

Citation: Li J X, Zhang S K, Xiao F, et al., A multi-tie points-based method for retrieving of the Arctic thin sea ice thickness from SMOS. Adv Polar Sci, 2026, 37(1): 43-55, doi: 10.12429/j.advps.2025.0043

1 Introduction

The exchange of heat, energy, mass, and momentum between the atmosphere and the ocean is influenced by sea ice (Kumar et al., 2021). The Arctic sea ice change has been very active in recent years, with the sea ice coverage shrinking and the sea ice thickness thinning, which is among the significant factors affecting global climate change (Laxon et al., 2013; MacDonald et al., 2005). The ocean–atmosphere heat exchange is dominated by thin ice less than 0.5 m (Maykut, 1978). Moreover, The Intergovernmental Panel on Climate Change (IPCC) expects that Arctic sea ice loss will continue through the middle of the century, along with a decline in sea ice extent and thickness (IPCC, 2023). Therefore, it is critical to retrieve the thin sea ice thickness accurately.

At present, two types of large-scale sea ice thickness retrieval methods are available. Satellite altimetry and remote sensing (including passive microwave and thermal infrared imagery) are primarily used to retrieve thick and

* Corresponding author. E-mail: zskai@whu.edu.cn

thin ice thicknesses, respectively. Altimetric sea ice thickness retrieval first identifies leads to calculate the freeboard and then obtains the sea ice thickness through the hydrostatic equilibrium equation (Laxon et al., 2003). Radar altimetry satellites, like ERS-1/2, ENVISAT, CryoSat-2 and ICESat series laser altimetry satellites, provide foundation data for retrieving sea ice thickness and other parameters. However, the sea ice thickness retrieved from satellite altimetry results in significant relative errors for thin ice (Laxon et al., 2003). One method of thin sea ice thickness retrieval is using the ice surface temperature from thermal infrared imagery (Mäkynen et al., 2013; Yu and Rothrock 1996), which requires clear skies, is heavily influenced by the weather, and can thereby result in vacancies and long-time intervals in the study area. Another method is the use of passive microwave data, which can penetrate clouds and is widely used in sea ice detection. An empirical equation is constructed based on the correlation between ice thickness and ice surface salinity to retrieve the ice thickness using a passive microwave in the 19–90 GHz band. However, this is only applicable for ice thickness of less than 10–20 cm (Martin et al., 2004; Naoki et al., 2008; Nihashi et al., 2009; Singh et al., 2011; Tamura and Ohshima, 2011; Tamura et al., 2007), which is insufficient for retrieving the polar thin sea ice thickness. The European Space Agency (ESA) launched the Soil Moisture and Ocean Salinity (SMOS) satellite in 2009. The satellite is equipped with the first Microwave Imaging Radiometer using Aperture Synthesis (MIRAS) at a frequency of 1.4 GHz (L-band). Using L-band, the thin sea ice thickness can be extracted due to higher penetration compared to 10–90 GHz, introducing a new method for retrieving the thin sea ice thickness and compensating for the altimetry satellite's shortcomings.

The microwave radiation of the target object is related to its physical properties, which is the basis for retrieving the sea ice thickness using passive microwave brightness temperature. Sea ice's microwave radiation energy differs from seawater due to its complex internal structure. Hence, the brightness temperature quickly identifies sea ice from seawater, increases with sea ice thickness, and gradually stabilizes. A three-layer medium model of the atmosphere–sea ice–seawater to verify the SMOS satellite's capacity to retrieve the sea ice thickness was constructed. Using aerial 1.4-GHz microwave radiometer observations with the semi-empirical algorithm, the retrieved maximum multi-year ice/first-year ice thickness of the Baltic Sea is 1.5 m/0.5 m, which is consistent with the sea ice thickness measured by electromagnetic induction. The ability of 1.4-GHz passive microwave brightness temperature to retrieve sea ice thickness was confirmed (Kaleschke et al., 2010). Multi-angle multi-polarization measurements have been released since the launch of the SMOS satellite (Kerr et al., 2010). To reduce the incident angle dependence in the retrieval of sea ice thickness, the incident angle is set to 0°–40° to calculate the first Stokes parameter (intensity) from the vertical and horizontal polarization components. The SMOS brightness temperature can retrieve the Arctic sea ice thickness according to the proposed semi-empirical algorithm (Kaleschke et al., 2012). However, the primary method assumes constant sea ice temperature and salinity, which is inconsistent with the natural Arctic environment. Tian-Kunze et al. (2014) improved the algorithm by introducing temperature, salinity variables, and a sea ice thickness distribution function, resulting in a more accurate thin sea ice thickness, which is in good agreement with the simulation system, the telemetry data, and the airborne electromagnetic data. In contrast to previous studies, Huntemann et al. (2014) used SMOS measurements with an incidence angle range of 40°–50° to calculate the polarization difference and intensity between the vertical and horizontal polarizations to construct an empirical algorithm to retrieve sea ice thickness, which can reach up to 0.5 m, based on the characteristic that different polarization brightness temperatures show different trends with the incidence angle. Ricker et al. (2017) integrated CryoSat-2 and SMOS to retrieve the weekly Arctic sea ice thickness, which was verified in the Barents Sea and compared with the airborne electromagnetic induction measurement. The results obtained from the fusion data are more accurate than those obtained from CryoSat-2. After the Soil Moisture Active Passive (SMAP) satellite was launched, Paţilea et al. (2019) provided a merged SMOS-SMAP sea ice thickness product with improved spatial and temporal coverage, while, the algorithm is an extension of the method proposed by Huntemann et al. (2014).

Passive microwave remote sensing technology has been gradually utilized to retrieve large-scale sea ice thickness because it is not affected by the weather. Kaleschke et al. (2010) selects a single-tie point (STP) pair to obtain the initial sea ice thickness based on the SMOS satellite's L-band penetration through sea ice, and Tian-Kunze et al. (2014) built a long-time series SMOS thin ice thickness product based on the initial sea ice thickness. The properties of seawater and sea ice vary around the Arctic, resulting in different values of seawater and sea ice tie points. Using the STP may lead to under/overestimation of sea ice thickness in other regions, and the properties of seawater and sea ice in the relevant regions can be reflected by partitioning the regions and selecting multi-tie point (MTP) pairs. In this study, we carried out the MTP for retrieving the sea ice thickness.

2 Data

2.1 SMOS brightness temperature

SMOS is a ESA-launched second-generation Earth exploration mission satellite that monitors soil moisture and ocean salinity. Since the summer of 2010, this satellite has been taking near real-time measurements and providing

multi-angle and multi-polarization data. The MIRAS is the only payload carried by the SMOS satellite, consisting of 69 evenly distributed individual antennas on three Y-shaped arms and has a working center frequency of approximately 1.4 GHz, a resolution of 30–50 km, and a swath of 900 km. MIRAS is the first synthetic aperture radiometer in orbit to use the L-band for observations. Every three days, the radiometer covers the entire globe, with a daily coverage in the polar regions (Kerr et al., 2001).

The SMOS L1C brightness temperature is used to retrieve thin ice thickness. The top of atmospheric (TOA) multi-angle brightness temperature of the SMOS L1C data is geographically located at the equal area discrete global grid system of ISEA 4h9 (Icosahedral Snyder Equal Area projection with aperture 4, resolution 9, and shape of cells as a hexagon), with a grid resolution of 15 km (Pinori et al., 2008). All brightness temperature and auxiliary data for each SMOS grid cell are collected during data processing, including the longitude, the latitude, the incident angle, the Faraday rotation angle, and the snapshot number.

SMOS measurements are influenced by radio frequency interference (RFI) while receiving microwave signals due to radar and radio transmissions (Mecklenburg et al., 2012). Meanwhile, the incident angle, the polarization mode, and ascending and descending orbits have an impact on the RFI (Camps et al., 2010). For simplicity, the threshold is utilized to distinguish the RFI in both horizontal and vertical polarization brightness temperatures. If any polarization observation in the snapshot exceeds 300 K, the snapshot is considered RFI contaminated and should be eliminated (Kaleschke et al., 2012; Tian-Kunze et al., 2014).

The first Stokes parameter (intensity) is nearly independent of the incidence angle within 0°–40°. This parameter is the average of the horizontal and vertical polarization brightness temperatures and is unaffected by the Faraday rotation. The intensity is also robust to the instrument and geophysical errors. The uncertainty produced by the transfer from the antenna reference frame to the Earth reference frame can be avoided using the intensity. Therefore, selecting the intensity to retrieve the sea ice thickness is preferred.

2.2 AMSR-E sea ice concentration

The AMSR-E microwave radiometer has a frequency band range of 6.9–89.0 GHz, 12 channels, a resolution of 5.4–56 km, and a scanning range of ±55°.

The National Snow and Ice Data Center (http://nsidc.org) provides Aqua/AMSR-E Arctic sea ice concentration (SIC) products. The AMSR-E SIC products, available from 4 May 2002 to 4 October 2011, are provided on polar stereographic projection at a 12.5-km grid resolution and a 1-d temporal resolution, and are obtained based on the Enhanced NASA Team (NT2) algorithm (Cavalieri et al., 2014; Markus and Cavalieri, 2000).

Based on SIC, seawater and sea ice are classified, and combined with brightness temperature time series, the tie-point values of seawater and sea ice are determined.

3 Methods

3.1 Brightness temperature observations

During the sea ice freezing period, we assume a spatially homogeneous ocean that is entirely covered by sea ice. Thus, the brightness temperature observed over sea ice is expressed as:

$$T_{\mathrm{obs}} = e_{\mathrm{ice}} T_{\mathrm{ice}} \tag{1}$$

where T_{obs} means the brightness temperature observations, e_{ice} means the sea ice emissivity and T_{ice} means sea ice physical temperature, in K. The sea ice emissivity with respect to sea ice thickness (d) is derived as follows (Kaleschke et al., 2024; Menashi et al., 1993).

$$e_{\mathrm{ice}} = \frac{(1-r_{\mathrm{i}})(1-Ar_{\mathrm{w}})}{1+Ar_{\mathrm{i}}r_{\mathrm{w}}+2\sqrt{r_{\mathrm{i}}r_{\mathrm{w}}}\cos(2\beta d)} \tag{2}$$

where r_{i} is the reflectivity of air to ice, and r_{w} is the reflectivity of sea ice to water; both are related to sea ice permittivity, and $A = \exp(-4\alpha d)$.

$$\alpha = \frac{\omega \cos\theta_{\mathrm{i}} \,|\, \mathrm{Im}\sqrt{\varepsilon_{\mathrm{ice}}}\,|}{c_0} \tag{3}$$

$$\beta = \frac{\omega \cos\theta_{\mathrm{i}}\, \mathrm{Re}\sqrt{\varepsilon_{\mathrm{ice}}}}{c_0} \tag{4}$$

β and α are the real and imaginary parts of sea ice attenuation coefficients, respectively. Both α and β have units of m^{-1}. Here, ω is the angular frequency, c_0 is the speed of light in vacuum, θ_{i} is the incidence angle, and $\varepsilon_{\mathrm{ice}}$ is the complex dielectric constant of sea ice.

Vant et al. (1978) proposed the empirical equation for calculating the dielectric constant of sea ice depending on relative brine volume V_{b} (in ‰, or per thousand) (Hu et al., 2023; Xie and Yan, 2024).

$$\varepsilon_{\mathrm{ice}} = a_0 + a_1 V_{\mathrm{b}} + j(a_2 + a_3 V_{\mathrm{b}}) \tag{5}$$

where j represents the imaginary part.

The coefficients for calculating the sea ice permittivity are presented in Table 1. The 1.4-GHz coefficients are interpolated linearly (Hallikainen and Winebrenner, 1992; Munoz-Martin et al., 2025), as shown in Table 1.

Table 1 Sea ice dielectric constant coefficient

Frequency/GHz	a_0	a_1	a_2	a_3
1.0	3.12	0.009	0.039	0.00504
1.4	3.10	0.0084	0.037	0.00445
2.0	3.07	0.0076	0.034	0.00356

Cox and Weeks (1983) proposed an equation for calculating the relative brine volume for low temperatures.

$$V_{\mathrm{b}}=\frac{\rho_{\mathrm{ice}}S_{\mathrm{ice}}}{F_1(T)-\rho_{\mathrm{ice}}S_{\mathrm{ice}}F_2(T)} \tag{6}$$

$$F_{i=1,2}=\sum_{j=0}^{3}\alpha_j T^j \tag{7}$$

$$\rho_{\mathrm{ice}}=0.917-1.403\times10^{-4}T_{\mathrm{ice}} \tag{8}$$

where ρ_{ice} is the density of sea ice in g·cm^{-3}, and S_{ice} represents the sea ice salinity expressed in density units (g·cm^{-3}). T (T_{ice}) is the sea ice temperature in ℃. The functions $F_1(T)$ and $F_2(T)$ are empirical temperature-dependent functions whose units are defined to ensure dimensional consistency of Equation (6), and are calculated using the polynomial coefficients listed in Table 2.

Table 2 Polynomial coefficients for the calculation of the relative brine volume under low temperatures

	T/℃	α_0	α_1	α_2	α_3
F_1	[−22.9, −2]	−4.732	−22.45	−0.6397	-1.074×10^{-3}
	[−30, 22.9)	9899	1309	55.27	0.716
F_2	[−22.9, −2]	-8.903×10^{-2}	-1.763×10^{-2}	-5.33×10^{-4}	8.801×10^{-6}
	[−30, −22.9)	8.547	1.089	0.04518	5.819×10^{-4}

Equation (2) is a coherent solution to sea ice emissivity. The periodicity of the emissivity relative to the sea ice thickness will be destroyed if the roughness (σ_{d}) (e.g., RMSD) of the sea ice thickness exceeds one-fourth of the applied electromagnetic wavelength, and an incoherent solution will be introduced (Menashi et al., 1993).

$$e_{\mathrm{ice}}=\frac{(1-r_{\mathrm{i}})(1-Ar_{\mathrm{w}})}{1-Ar_{\mathrm{i}}r_{\mathrm{w}}}\left[\frac{1-\sqrt{Ar_{\mathrm{i}}r_{\mathrm{w}}}\exp(-\beta\sigma_{\mathrm{d}})}{1+\sqrt{Ar_{\mathrm{i}}r_{\mathrm{w}}}\exp(-\beta\sigma_{\mathrm{d}})}\right] \tag{9}$$

Under the typical Arctic condition, Equations (2) and (9) are simulated under various sea ice thicknesses. The coherent emissivity has a significant periodicity, a single emissivity corresponds to diverse sea ice thicknesses, and the incoherent emissivity increases and tends to stabilize with the sea ice thickness, which is suitable for retrieving thin ice thicknesses, as shown in Figure 1. The roughness is set to an empirical value of 20 cm and a fixed percentage of sea ice thickness (0.1 d) in the incoherent emissivity. When the sea ice thickness is zero, the sea ice emissivity produced by applying a constant sea ice thickness roughness is inconsistent with the open water emissivity because roughness is 0 when there is no sea ice, and when the sea ice thickness roughness increases, 0.1 d should be introduced as the sea ice thickness roughness.

3.2 Sea ice thickness retrieval

Equations (1) to (7) are simple expressions for the ground microwave radiation received by SMOS. According to the semi-empirical approach proposed by Kaleschke et al. (2010).

$$T_{\mathrm{obs}}=T_1-(T_1-T_0)\exp(-\gamma d) \tag{10}$$

$$d=-\frac{1}{\gamma}\ln\left(\frac{T_1-T_{\mathrm{obs}}}{T_1-T_0}\right) \tag{11}$$

where sea ice tie-point value (T_1) means the brightness temperatures of infinitely thick sea ice, seawater tie-point value (T_0) means the brightness temperatures of open water, the tie-point pair is chosen from the same grid cell before and after the freeze-up, and the attenuation factor (γ), the least squares optimization is constructed by combining Equations (1) and (9) to obtain γ for the retrieval of the sea ice thickness.

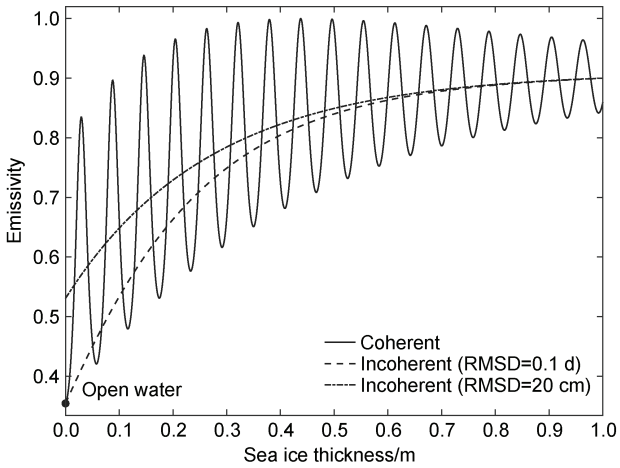

Figure 1 Corresponding coherent and incoherent sea ice emissivity values for various sea ice thicknesses.

Equations (4) and (6) show that some sea ice parameters, such as sea ice temperature and sea ice salinity, are required in the process of retrieving the sea ice thickness. Specific locations are selected as the tie points during the sea ice freezing period, the brightness temperature time series is constructed, the seawater and sea ice tie-point values are derived, and the Arctic sea ice thickness is obtained by simultaneously using Equations (1) and (10) (Kaleschke et al., 2010, 2012).

3.3 Tie points selection

The retrieval of sea ice thickness by STP has several restrictions. The properties (e.g., salinity, temperature) of seawater and sea ice in different regions are not consistent, which leads to the inconsistency of T_0 and T_1. As a result, using a STP to retrieve sea ice thickness may not fully reflect the sea ice thickness characteristics in different regions.

Due to the lack of spatiotemporal applicability when using a STP in sea ice thickness retrieval process, resulting in significant uncertainty in the retrieved sea ice thickness away from the tie point, therefore, this study extracted MTP with scene adaptability to jointly retrieve sea ice thickness.

The first issue we must address is how to choose MTPs. We should know the T_0 at the beginning of the freezing stage and the T_1 at the end of the freezing stage within the

same grid cell. Some issues in the study area which is the same as Kaleschke et al. (2012) will be encountered if the areas are evenly divided by geography graticule. For example, multiyear ice areas only have sea ice tie-point values; similarly, if sea areas have not frozen, only seawater tie-point values exist. As a result, multiyear ice and perennial seawater areas should be avoided, the long-term sea ice brightness temperature and SIC time series should be constructed in a point-by-point manner, and points that are severely affected by dynamics, such as sea ice drift and wind fields, should be eliminated. To identify stable ice tie points, a statistical hypothesis test was applied to the brightness temperature time series. Specifically, a one-sample *t*-test was performed at the 5% significance level. The null hypothesis H_0 assumes that the mean brightness temperature of the window is equal to the fitted sea ice tie-point value, while the alternative hypothesis H_1 assumes a significant deviation from this value. Only brightness temperature time series for which the null hypothesis could not be rejected were retained as valid sea ice tie points, whereas brightness temperature time series showing statistically significant deviations were excluded from further analysis.

4 Results and discussion

Different tie points are selected; empirical parameters under a typical Arctic environment, such as bulk sea ice temperature T_{ice}=−7 ℃ and sea ice salinity S_{ice}=8 g·kg^{-1}, are applied; the sea ice thickness on 15 November, 2010, is retrieved; and the difference between the sea ice thicknesses retrieved by STP and MTP is investigated.

4.1 Sea ice thickness retrieval of different tie points

The sea ice thickness retrieved by deriving the seawater and sea ice tie-point values on the basis of the time series of brightness temperature at different grid cells is shown in Figure 2. Figure 2a depicts the sea ice thickness derived from earlier studies of STP (Kaleschke et al., 2012), 77.5°N and 137.5°E. Figures 2b and 2c show the sea ice thickness derived from the tie point grid cells at 80.7°N, 72.7°E and 79.0°N, and 153.6°E, respectively. The overall sea ice thickness is lower in Figure 2b than in Figure 2a, and higher in Figure 2c than in Figure 2a.

The brightness temperature time series and the SIC during the sea ice freezing period are shown in Figure 3. During the sea ice freezing period, the sea ice grows, and the SIC increases more rapidly than the sea ice brightness temperature. The SIC reaches 100% within a short time, the sea ice brightness temperature is not synced, and the sea ice brightness temperature continues to increase and gradually tends to stabilize.

However, the sea ice thickness increase varies by region. The STP grid cell locates at 77.5°N, 137.5°E in Figure 3a, where T_0 is (105.4±1.1) K. On 20 October, 2010, sea ice appeared, and the SIC reached 100% on 28 October, while the sea ice brightness temperature continued to rise, eventually stabilizing at (247.2±1.1) K. The maximum sea ice thickness retrieved was 0.56 m. The STP grid cell in Figure 3b is at 80.7°N, 72.7°E, where T_0 is (101.3±1.1) K,

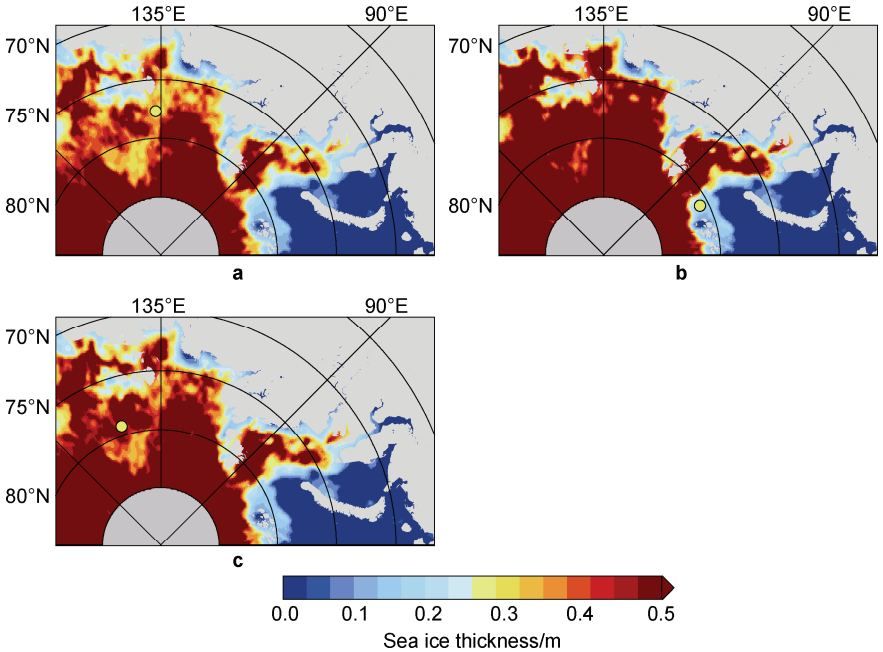

Figure 2 Sea ice thickness retrieved according to different tie points on 15 November, 2010. **a**, **b** and **c** show the tie point grid cells at 77.5°N, 137.5°E; 80.7°N, 72.7°E; and 79.0°N, 153.6°E, respectively. The yellow circles are the locations of the tie point grid cells.

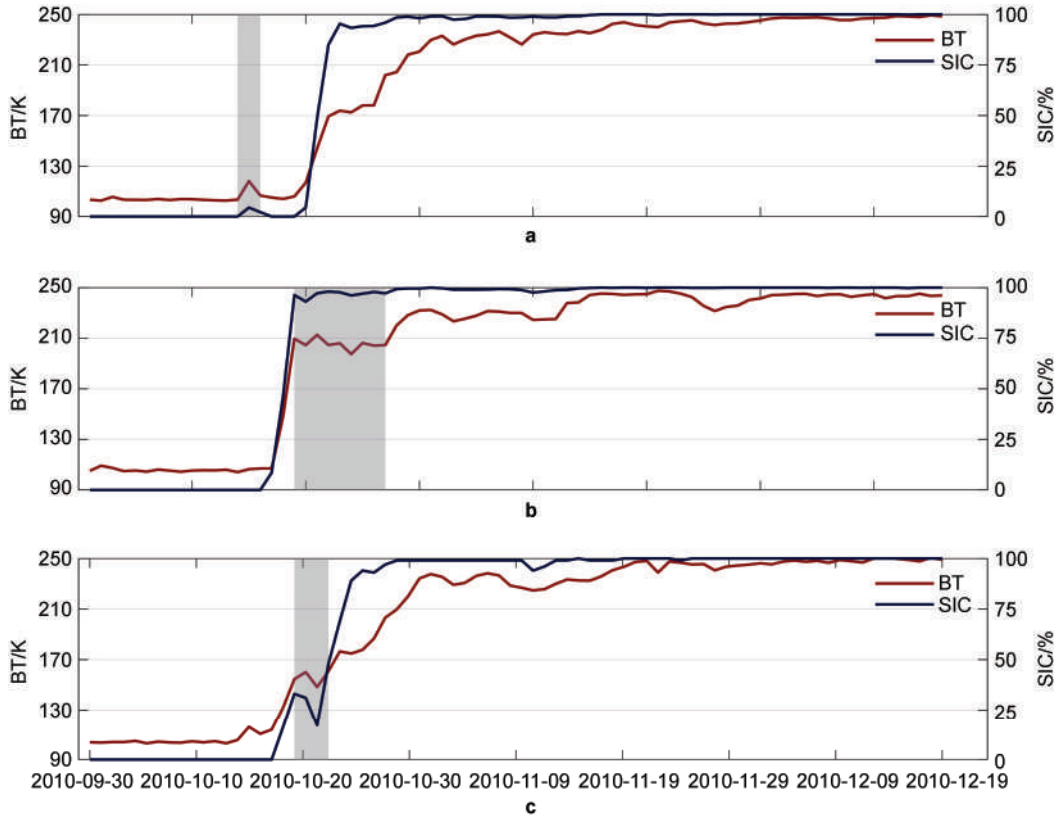

Figure 3 Time series of sea ice brightness temperature (BT) and SIC at different grid cells: **a**, 77.5°N, 137.5°E; **b**, 80.7°N, 72.7°E; **c**, 79.0°N, 153.6°E. The shade represents the dynamic effect and should be ignored for retrieving sea ice thickness.

1,327 km away from the STP grid cell in Figure 3a. Sea ice appeared later, on 17 October. On 30 October, the SIC reached 100%, and the sea ice brightness temperature continued to increase, eventually stabilizing at (240.3±1.7) K. The maximum sea ice thickness retrieved was 0.48 m. The STP grid cell in Figure 3c is at 79.0°N, 153.6°E, 400 km away from the STP grid cell in Figure 3a, where T_0 is (103.5±0.6) K and sea ice appeared sooner, for the first time on 11 October, and the SIC reached 100% on 31 October. The sea ice brightness temperature progressively increased, and T_1 is (245.2±1.0) K. The maximum retrieved sea ice thickness was 0.59 m.

Table 3 shows the Arctic sea ice thickness on 15 November, 2010, according to different tie points. Figures 3b, 3c, and 3a show the largest sea ice thickness areas, from large to small; the maximum sea ice thickness is 0.48, 0.59, and 0.56 m, respectively; the corresponding average sea ice thickness is 0.37, 0.40, and 0.36 m, respectively. This result can be attributed to the inconsistency of the T_0 and T_1 derived from the time series of brightness temperature at different grid cells and the sea ice thickness.

The shaded parts in Figure 3 represent the dynamic effect, which causes sudden accumulation or breach of sea ice and sudden changes in SIC and brightness temperature. However, the thermodynamic growth of sea ice is given more weight in the retrieval of sea ice thickness. The sea ice bright temperature increases with the reduction in temperature, freezing of sea ice, and increase in thickness during the sea ice freezing phase and gradually tends to stabilize. Thus, we ignore the abrupt shift in sea ice brightness temperature produced by dynamics when retrieving the sea ice thickness.

Table 3 Arctic sea ice thickness retrieved from different STPs on 15 November, 2010

No.	Location	Seawater tie-point value T_0/K	Sea ice tie-point value T_1/K	Average sea ice thickness /m	Maximum sea ice thickness /m	Grid cells with maximum sea ice thickness
a	77.5°N,137.5°E	105.4±1.1	247.2±1.1	0.36	0.56	7,159
b	80.7°N, 72.7°E	101.3±1.1	240.3±1.7	0.37	0.48	13,933
c	79.0°N, 153.6°E	103.5±0.6	245.2±1.0	0.40	0.59	9,013

4.2 Results and analysis of sea ice thickness by MTPs

The impact of different STPs on sea ice thickness retrieval is discussed in the previous section. Multiple STPs are selected to construct MTP to retrieve sea ice thickness. In the experimental area, a total of 1,230 tie points are present according to the selected rules. Four kinds of MTP combinations are selected for SIT retrieval, as shown in Figure 4. The first three tie point combinations are included in all 1,230 tie points.

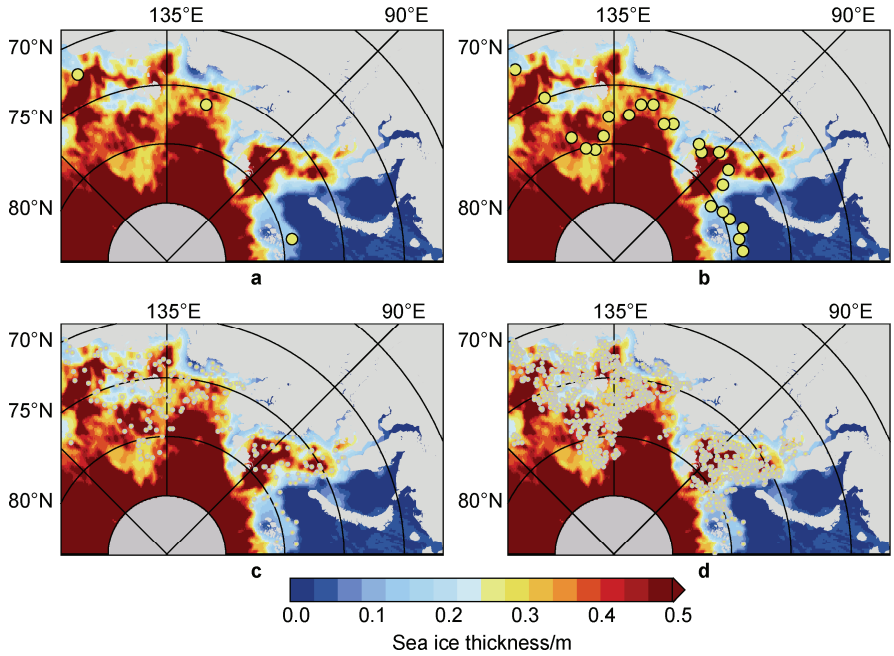

Figure 4 Distribution of different MTP combinations. **a**, 3-tie points; **b**, 23-tie points; **c**, 230-tie points; **d**, 1,230-tie points.

According to different MTP combinations, the SIT is jointly retrieved via the weighted averaging method, the inverse-distance weighting method was used to calculate the sea ice thickness at grid points based on the distances to the selected tie points. The distance between each grid point and the tie points was calculated using spherical distance (i.e., the great-circle distance on the Earth's surface). The weight was then computed as the inverse of the distance squared. Although the runtime of the MTP-based thickness retrieval itself is relatively short, the dominant computational cost arises from the tie-point selection procedure, which involves quality control, dynamic filtering, and statistical testing for each candidate tie point. In practice, the average processing time required to identify a single tie point is approximately 5 min. As a result, the total preprocessing time increases rapidly with the number of tie points, from minutes for MTP_3 to several days for MTP_1230. Given that the retrieval accuracies of MTP_23, MTP_230, and MTP_1230 are comparable, MTP_230 represents a practical compromise between retrieval accuracy and preprocessing efficiency. As shown in Figure 5, the different MTP combinations reveals yield similar SIT patterns, indicating the robustness of the proposed method when identifying the major ice regions. Small local differences may be observed, but the overall ice distribution pattern remains consistent.

The results reveal that the process of jointly retrieving SIT via MTPs is influenced by the nearby tie points. In addition, the STP grid cell in Figure 2a is located in the Laptev Sea, resulting in a small difference in the area. While consistency is exhibited by the overall ice distributions of different MTP combinations, the selected combination can still influence the precision of the final SIT estimates.

We compare the MTP SIT and the original STP SIT with SIT products, yielding the following results. Tables 4 and 5 present comparisons between the retrieved SIT (from STP/MTP) and two reference products: SIT_BREMEN (below 0.51 m) and SIT_AWI (below 0.6 m). For the SIT_BREMEN, the maximum retrievable thickness is limited to 0.5 m, and values exceeding this limit are capped at 0.51 m. For the SIT_AWI, a threshold of 0.6 m is applied. Sensitivity tests using alternative thresholds (0.5 m, 0.6 m, and 0.7 m) indicate that although the absolute values of mean bias difference (MBD) and root mean square difference (RMSE) vary slightly with the chosen cutoff, the relative performance of the retrieval methods remains unchanged. In all cases, MTP-based retrievals consistently outperform the STP approach, demonstrating that the conclusions of this study are not sensitive to the specific choice of the thin ice thickness threshold. Compared with SIT_BREMEN, the MBD ranges from −0.063 m (STP_a) to −0.024 m (MTP_230). Compared with the reference, all the combinations slightly underestimate the SIT, but the MTPs perform better than the STP does. MTP_230 shows perfect agreement, whereas MTP_1230 exhibit small, nearly identical underestimations; the RMSE decreases from 0.093 m (STP_a) to a range from 0.073 m to 0.056 m with different MTP combinations. The RMSE reflects the same pattern observed in the MBD. MTP_230 yields the smallest error, followed by MTP_1230 and MTP_23. STP_a has the highest error, indicating that the STP is less accurate in terms of estimating SIT. Similarly, in the SIT_AWI comparison, the MBD improves from −0.097 m (STP_a) to a range from −0.080 m to −0.063 m with MTP combinations; while these values are slightly greater than

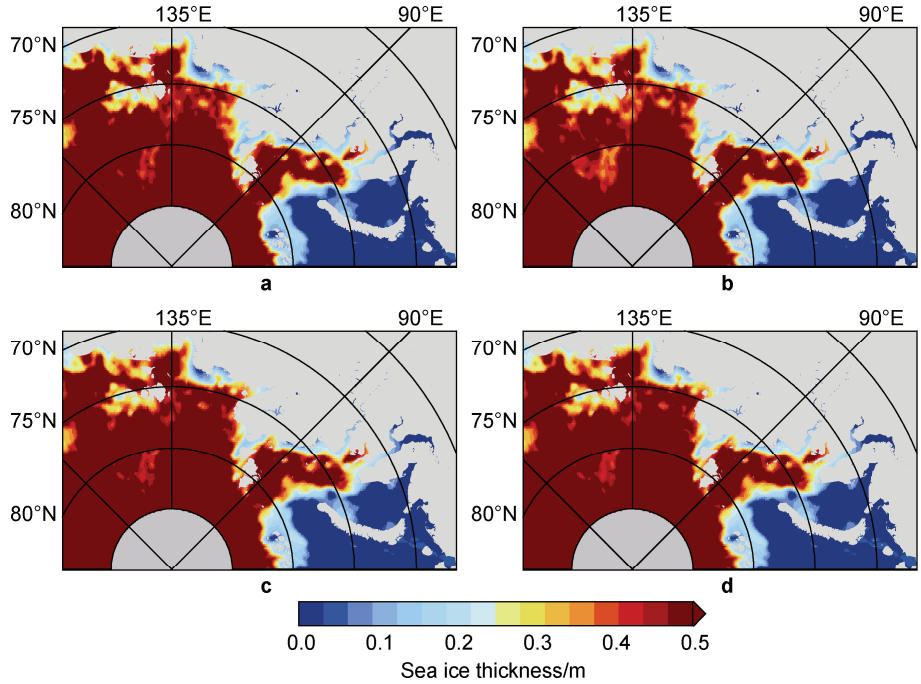

Figure 5 Sea ice thickness obtained by different MTP combinations. **a**, 3-tie points; **b**, 23-tie points; **c**, 230-tie points; **d**, 2,300-tie points.

those in the SIT_BREMEN comparison, the trend still shows a reduction in bias with more tie points. The RMSE also decreases from 0.154 m (STP_a) to a range from 0.135 m to 0.115 m. In contrast, the MTP results demonstrate superior MBD and RMSE in comparison with those of the STP. Among the MTP combinations, MTP_230 is the most accurate option across both references, with MTP_23 and MTP_1230 providing similar performance. These three MTP combinations are equivalent in terms of precision, especially compared with the STP, which induces larger errors.

For both comparisons, as the number of tie points increases, both the MBD and the RMSE exhibit overall decreasing trends. This suggests that adding more tie points improves the accuracy of SIT retrieval. However, after a certain number of points (approximately MTP_23 and MTP_1230), the MBD and RMSE improvements begin to stabilize. This indicates that while adding more points helps improve the achieved accuracy, there is a limit after which additional tie points yield diminishing returns.

Although Tables 4 and 5 show clear reductions in MBD and RMSE from STP to MTP, these metrics alone do not indicate whether the observed improvements are statistically significant. Therefore, paired *t*-tests were conducted at the grid-cell level using absolute retrieval errors to evaluate the robustness of the performance improvements.

As summarized in Table 6, all MTP configurations yield positive mean error reductions relative to STP for both SIT_BREMEN and SIT_AWI. The corresponding 95% confidence intervals do not include zero, and the *p*-values are all below 0.01, indicating that the improvements from STP to MTP are statistically significant. These results confirm that the reductions in RMSE and MBD reported above reflect a systematic improvement rather than random variability.

Table 4 Comparison among the SIT obtained by the STP and MTP with SIT_BREMEN below 0.51 m on 15 November, 2010

	STP_a	MTP_3	MTP_23	MTP_230	MTP_1230
MBD/m	−0.063	−0.043	−0.032	−0.024	−0.025
RMSE/m	0.093	0.073	0.063	0.056	0.056

Table 5 Comparison among the SIT obtained by the STP and MTP with SIT_AWI below 0.6 m on 15 November, 2010

	STP_a	MTP_3	MTP_23	MTP_230	MTP_1230
MBD/m	−0.097	−0.080	−0.069	−0.063	−0.063
RMSE/m	0.154	0.135	0.123	0.115	0.116

In the experiment, considering both efficiency and accuracy, we select the 23-tie point combination as an example to analyze the advantages of MTPs in sea ice thickness retrieval tasks. Figure 6 indicates that the minimum and maximum distances between each pair of tie points are 80.5 km and 457.9 km, respectively, with an average distance of 176.5 km. The details of MTP_23 are presented in Table 7, where Max (*d*) is the maximum retrieved sea ice thickness corresponding to each tie point. The brightness temperature and SIC time series of each tie point are displayed during the sea ice freezing period, and the results are shown in Figure 7.

Table 6 Statistical significance of the performance improvement from STP to MTP based on paired *t*-tests of grid-cell absolute errors. Results are shown for comparisons against the SIT_BREMEN (<0.51 m) and SIT_AWI (<0.6 m)

STP-MTP comparison (MTP configuration)	MeanD/m		95% CI/m		*p*-value	
	SIT_BREMEN	SIT_AWI	SIT_BREMEN	SIT_AWI	SIT_BREMEN	SIT_AWI
MTP_3	0.016	0.013	[0.016, 0.017]	[0.013, 0.014]	<0.01	<0.01
MTP_23	0.024	0.021	[0.023, 0.024]	[0.020, 0.021]	<0.01	<0.01
MTP_230	0.029	0.026	[0.029, 0.030]	[0.025, 0.027]	<0.01	<0.01
MTP_1230	0.029	0.025	[0.028, 0.029]	[0.024, 0.026]	<0.01	<0.01

Note: MeanD denotes the mean difference between the absolute errors of STP and MTP (|e_STP|−|e_MTP|), evaluated against the same reference product.

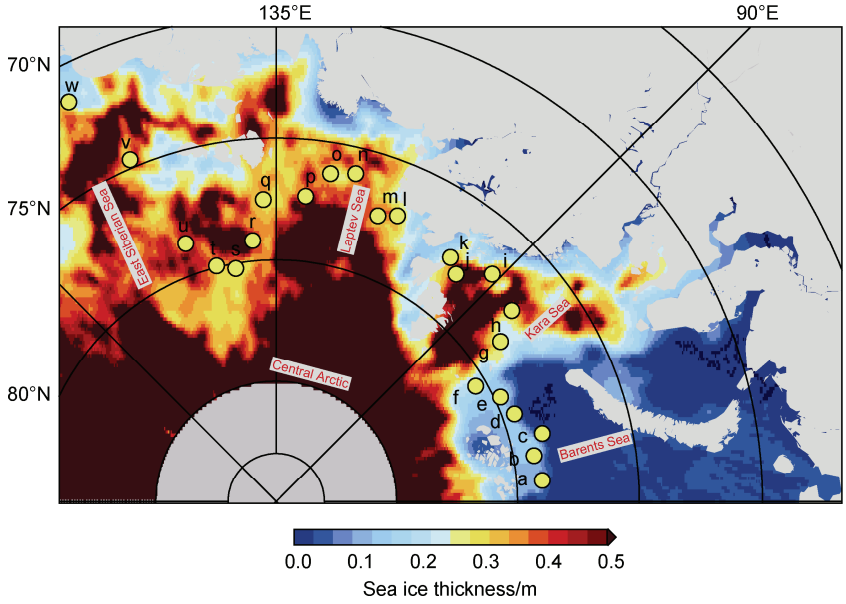

Figure 6 The distribution of the 23-tie points, where the yellow circles represent the locations of the MTPs. The base map shows the retrieved Arctic sea ice thickness from Figure 4a.

As shown in Table 7, the tie point grid cells are not selected in some areas because to obtain T_0 and T_1, the time series of seawater brightness temperature and high SIC sea ice brightness temperature should both exist at the beginning and end of the freezing period, as shown in Figure 3. However, some areas cannot satisfy the requirements. The brightness temperature and SIC time series of each MTP are displayed during the sea ice freezing period, and the results are shown in Figure 7.

Table 7 and Figure 7 show certain commonalities in the time series of sea ice brightness temperature and SIC between adjacent tie points. However, the time series at each location differ because the study area encompasses the maritime areas.

The tie point grid cells in Figures 7a–7c are located in the Barents Sea. Among all the tie points, sea ice began to freeze latest, appeared for the first time on 1 November, 2010, and was affected by the dynamics on 12 November. The pattern shown in Figure 7c is the most significant, followed by Figures 7a and 7b, resulting in the decrease of sea ice brightness temperature and SIC. The SIC reached the maximum after the decline, while the brightness temperature continued to rise. The brightness temperature stabilized at (235.6±1.75) K in Figure 7c, while the sea ice brightness temperature declined with the SIC on 26 and 24 November in Figures 7a and 7b and varied substantially before stabilizing at (237.66±1.82) K and (239.09±1.38) K, respectively. The sea ice brightness temperature and SIC declined again under the influence of dynamics on 12 December, as shown in Figure 7c, and stabilized on 21 December.

In Figures 7d–7k, the tie point grid cells are located in the Kara Sea. Since the first appearance of the corresponding sea ice (1 November, 1 November, 30 October, 28 October, 20 October, 7 October, 7 October, 5 October), which demonstrated that the speed of sea ice freezing gradually accelerates, and sea ice appears earlier and earlier. As we can see, the sea ice brightness temperature and SIC growth curves are similar within different tie point grid cells, but the sea ice thickness derived is different, as shown in Table 7, reflecting the limitations of STP retrieval. For example, the dynamics affected tie points d and e (Figures 7d and 7e) on 18 October, causing the brightness temperature to rise, in contrast, tie point d (Figure 7d) was more influenced. The sea ice brightness temperature and the SIC increased

Table 7 Information concerning the MTPs used to retrieve sea ice thicknesses

No.	Grid cells	T_0/K	T_1/K	Max (d)/m
a	78.9°N, 49.5°E	103.43	237.66	0.58
b	79.2°N, 55.1°E	103.33	239.09	0.55
c	78.6°N, 59.4°E	101.97	235.60	0.58
d	79.5°N, 65.2°E	103.44	239.44	0.53
e	79.7°N, 70.0°E	102.05	241.76	0.54
f	80.5°N, 75.1°E	104.88	237.24	0.52
g	78.6°N, 80.5°E	104.18	236.79	0.57
h	77.5°N, 84.0°E	104.36	237.80	0.60
i	77.0°N, 91.4°E	103.76	241.22	0.59
j	78.0°N, 96.6°E	106.49	245.75	0.58
k	77.6°N, 99.5°E	104.99	241.93	0.52
l	77.2°N, 112.0°E	106.44	245.81	0.53
m	77.5°N, 115.4°E	105.73	243.88	0.57
n	76.0°N, 121.4°E	104.80	244.60	0.52
o	76.3°N, 125.6°E	102.97	244.70	0.54
p	77.3°N, 129.5°E	102.70	242.42	0.57
q	78.7°N, 135.3°E	102.79	243.74	0.52
r	79.2°N, 140.2°E	102.43	245.55	0.61
s	80.2°N, 144.9°E	102.70	244.66	0.60
t	79.9°N, 149.3°E	102.81	244.89	0.57
u	78.7°N, 154.4°E	104.48	244.46	0.56
v	74.7°N, 158.2°E	105.30	243.45	0.55
w	71.4°N, 162.4°E	103.33	239.68	0.58

rapidly after 1 November. The sea ice brightness temperature and the SIC declined dramatically on 12 November, and then the SIC reached its maximum. The sea ice brightness temperature increased and was stable at (239.44±1.76) K and (241.46±1.27) K. The tie point grid cells in Figures 7h–7k are in the Kara Sea's east and are considerably influenced by the dynamics. Sea ice in Figure 7h appeared earlier than that in Figure 7g and suffered from dynamic effects. In Figure 7h, sea ice accumulated on 13 October, and the sea ice brightness temperature and SIC rose. Meanwhile, Figure 7i shows that sea ice broke, and the sea ice brightness temperature and the SIC suddenly declined on 13 October because of the dynamics, and there is a difference between the two sea ice tie points.

The tie point grid cells in Figures 7l to 7r are located in the Laptev Sea. The figures show that sea ice first appeared (20 October, 19 October, 16 October, 15 October, 13 October, 13 October, 14 October). The trend is consistent with the Kara Sea; from west to east, sea ice appeared earlier and earlier, and the rate of sea ice freezing increased, with the exception of the tie point shown in Figure 7r, gradually accelerating to one day earlier than the preceding one. Unlike tie point l (Figure 7l), tie point m (Figure 7m) is significantly affected by the dynamics in the early stage before the sea ice appearance. Sea ice began to accumulate on 9 October, resulting in a sudden increase in the sea ice brightness temperature and SIC, and then sea ice appeared on 19 October and gradually grew. No substantial change in sea ice occurred throughout the later period of sea ice freezing once the SIC reached 100%. The sea ice brightness temperatures stabilized at (245.81±1.48) K and (243.88±1.23) K. The sea ice brightness temperature then declined on 30 November, with the decrease at tie point l (Figure 7l) being particularly noticeable. The brightness temperature increased and dropped again on 22 December. The rest tie point grid cells are similar in sea ice growth, for example, the tie point grid cells in Figures 7p to 7r are in the northeast of the Laptev Sea. These areas are insignificantly affected by the dynamics, and the first occurrence time of sea ice is similar. The sea ice brightness temperature in the later stages of sea ice freezing is (242.42±1.77) K, (243.74±2.06) K, and (245.55±1.86) K, respectively, and the sea ice brightness temperature dropped on 17 December.

In Figures 7s–7w, the tie point grid cells are located in the East Siberian Sea. The tie point grid cells of Figures 7s and 7t are in the northwest of the East Siberian Sea and near the Laptev Sea. Therefore, they are insignificantly affected by the dynamics like shown in Figure 7r. However, both sea ice first appeared on 21 October uniformly, later than that shown in Figure 7r. Figure 7t is similar with Figure 7s. Sea ice first appeared on 7 October, as seen in Figure 7u. During sea ice growth, the sea ice brightness temperature and SIC decreased simultaneously on 17 October. Then, the SIC increased, reaching the maximum on 23 October, while the sea ice brightness temperature continued to rise, with the sea ice tie-point value of (244.66±1.12) K. The tie point grid cell in Figure 7v is 458 km away from the STP grid cell in Figure 7u; the first appearance of sea ice occurred around the same time, that is, on 8 October. The tie point grid cell in Figure 7w is 383 km away from the tie point in Figure 7v and is located near the coast. On 13 October, sea ice emerged initially. Given the dynamics, the sea ice brightness temperature dropped on 12 November and subsequently stabilized at (239.68±1.92) K.

The dynamics have varied effects on different locations in the same sea region, as shown in Table 7 and Figure 7. Furthermore, the brightness temperature time series at different locations are inconsistent with the SIC time series, resulting in different seawater and sea ice tie-point values. Furthermore, the retrieved sea ice thickness is inconsistent due to the different properties of seawater and sea ice in different regions. This finding demonstrates that utilizing MTPs to retrieve the sea ice thickness is more rational than using the STP. For tie point grid cells 80.5°N, 75.1°E and 79.2°N, 140.2°E, the differences between the T_0 and T_1 are 2.45 and 8.31 K, respectively. If the sea ice thickness is retrieved by tie point 80.5°N, 75.1°E, then the sea ice thickness of the other areas will be underestimated;

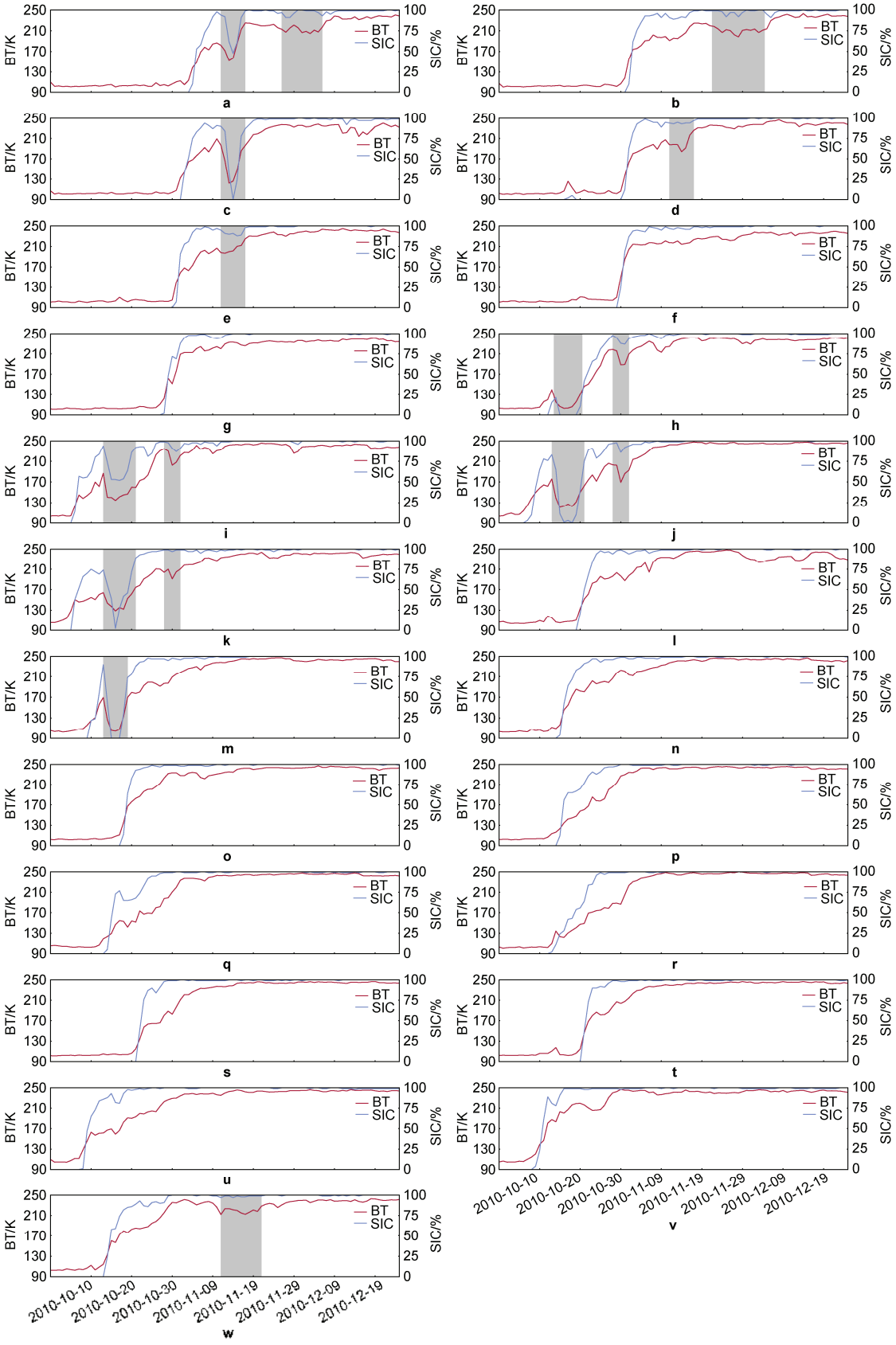

Figure 7 Sea ice BT and SIC time series. The sequences in the figure correspond to those in Table 7, and the shaded parts are consistent with those in Figure 3. **a**–**w** present the data for tie point grid cells a–w in Figure 6, respectively.

and at the tie point in the Barents Sea at 78.6°N, 59.4°E, the sea ice in other sea areas will begin to freeze earlier if the STP is utilized to retrieve the sea ice thickness because T_0 is lower than others. Therefore, according to the MTPs and their corresponding areas, the sea ice thickness on 15 November, 2010 is retrieved, as shown in Figure 7. Several marine areas near the coast in the Laptev Sea and the Northland Islands are not frozen, in addition to parts of the Barents Sea and the Kara Sea.

5 Conclusions

The SMOS microwave brightness temperature can be used to retrieve the thin sea ice thickness. The seawater and sea ice tie-point values were determined based on the brightness temperature observation and SIC time series at the STP grid cell to retrieve the sea ice thickness using the semi-empirical approach. However, for large-scale areas, the STP cannot reflect the entire region's properties, leading to under/overestimation of sea ice thickness in other regions, the retrieval has certain limitations.

MTPs are different from STPs in terms of retrieving SIT, and the accuracy of the SIT retrieved from MTPs is greater than that retrieved from STPs, revealing more details. Among all the MTP combinations, MTP_230 was the most accurate option across both SIT, with MTP_23 and MTP_1230 providing similar performances. These three combinations had nearly the same level of precision, indicating that when the number of tie points reached 23 or more, the system became sufficiently stable, and further increasing the number of tie points did not significantly improve the resulting accuracy. Considering both retrieval accuracy and the computational cost associated with tie-point selection, MTP_230 provides a practical balance between efficiency and performance. Specifically, the proposed approach can not only demonstrate the variations exhibited by the properties of seawater and sea ice in different regions but also provide more accurate estimates of the initial freezing time and maximum SIT at different scales.

Due to the different properties of seawater and sea ice in each sea area, the sea ice freezing period varies, but all properties show a trend of accelerating sea ice freezing from west to east. Furthermore, the sea ice brightness temperature and SIC time series at different tie points, and the retrieved sea ice thickness are inconsistent with each other.

In this study, the MTP method was primarily validated using data from the sea ice freezing period. The applicability and accuracy of the MTP method during the summer thawing or warming season, when sea ice properties may significantly change due to temperature fluctuations and melting, were not evaluated. This remains a limitation of the current approach, and further research is needed to assess its performance under these dynamic conditions.

Data availability statement The SMOS passive microwave brightness temperature is provided by the European Space Agency (https://smos-diss.eo.esa.int/oads/access/collection/SMOS_Open_V7). AMSR-E passive microwave sea ice concentration products are available at https://nsidc.org/data/AESI12/versions/3.

Acknowledgements This work was supported by the National Key Research and Development Program of China (Grant nos. 2023YFC2809103, 2024YFC2813505), the Fundamental Research Funds for the Central Universities (Grant nos. 2042025kf0083, 2042025gf0014), and the Antarctic Zhongshan Ice and Space Environment National Observation and Research Station (Grant no. ZSNORS-20252702).

References

Camps A, Gourrion J, Tarongi J M, et al. 2010. Rfianalysis in SMOS imagery. 2010 IEEE International Geoscience and Remote Sensing Symposium. Honolulu: IEEE, 2007–2010, doi:10.1109/IGARSS.2010.5654268.

Cavalieri D J, Markus T, Comiso J C. 2014. AMSR-E/Aqua daily l3 12.5 km brightness temperature, sea ice concentration, & snow depth polar grids. (AE_SI12, Version 3). [2025-10-10]. Boulder, Colorado USA. NASA National Snow and Ice Data Center Distributed Active Archive Center, doi:10.5067/AMSR-E/AE_SI12.003.

Cox G F N, Weeks W F. 1983. Equations for determining the gas and brine volumes in sea-ice samples. J Glaciol, 29(102): 306-316, doi:10.3189/s0022143000008364.

Hallikainen M, Winebrenner D P. 1992. The physical basis for sea ice remote sensing. Geophys Monog Series, 68: 29-46, doi: 10.1029/GM068p0029.

Hu Y, Jiang Z H, Liu W, et al. 2023. GNSS-R sea ice detection based on linear discriminant analysis. IEEE Trans Geosci Remote Sensing, 61: 1-12, doi:10.1109/tgrs.2023.3269088.

Huntemann M, Heygster G, Kaleschke L, et al. 2014. Empirical sea ice thickness retrieval during the freeze-up period from SMOS high incident angle observations. Cryosphere, 8(2): 439-451, doi:10.5194/tc-8-439-2014.

Intergovernmental Panel on Climate Change (IPCC). 2023. Summary for policymakers//Climate change 2021–the physical science basis: Working Group I contribution to the sixth assessment report of the Intergovernmental Panel on Climate Change. Cambridge: Cambridge University Press,1-2, doi: 10.1017/9781009157896.

Kaleschke L, Maaß N, Haas C, et al. 2010. A sea-ice thickness retrieval model for 1.4 GHz radiometry and application to airborne measurements over low salinity sea-ice. Cryosphere, 4(4): 583-592, doi:10.5194/tc-4-583-2010.

Kaleschke L, Tian-Kunze X, Maaß N, et al. 2012. Sea ice thickness retrieval from SMOS brightness temperatures during the Arctic freeze-up period. Geophys Res Lett, 39(5): 2012GL050916, doi:10.1029/2012GL050916.

Kaleschke L, Tian-Kunze X, Hendricks S, et al. 2024. SMOS-derived Antarctic thin sea ice thickness: data description and validation in the Weddell Sea. Earth Syst Sci Data, 16(7): 3149-3170, doi:10.5194/essd-16-3149-2024.

Kerr Y H, Waldteufel P, Wigneron J P, et al. 2001. Soil moisture retrieval from space: the Soil Moisture and Ocean Salinity (SMOS) mission.

IEEE Trans Geosci Remote Sens, 39(8): 1729-1735, doi:10.1109/36.942551.

Kerr Y H, Waldteufel P, Wigneron J P, et al. 2010. The SMOS mission: new tool for monitoring key elements ofthe global water cycle. Proc IEEE, 98(5): 666-687, doi:10.1109/JPROC.2010.2043032.

Kumar A, Yadav J, Mohan R. 2021. Spatio-temporal change and variability of Barents-Kara sea ice, in the Arctic: ocean and atmospheric implications. Sci Total Environ, 753: 142046, doi:10.1016/j.scitotenv.2020.142046.

Laxon S, Peacock N, Smith D. 2003. High interannual variability of sea ice thickness in the Arctic region. Nature, 425(6961): 947-950, doi:10.1038/nature02050.

Laxon S W, Giles K A, Ridout A L, et al. 2013. CryoSat-2 estimates of Arctic sea ice thickness and volume. Geophys Res Lett, 40(4): 732-737, doi:10.1002/grl.50193.

MacDonald R W, Harner T, Fyfe J. 2005. Recent climate change in the Arctic and its impact on contaminant pathways and interpretation of temporal trend data. Sci Total Environ, 342(1-3): 5-86, doi:10.1016/j.scitotenv.2004.12.059.

Mäkynen M, Cheng B, Similä M. 2013. On the accuracy of thin-ice thickness retrieval using MODIS thermal imagery over Arctic first-year ice. Ann Glaciol, 54(62): 87-96, doi:10.3189/2013aog62a166.

Markus T, Cavalieri D J. 2000. An enhancement of the NASA Team sea ice algorithm. IEEE Trans Geosci Remote Sens, 38(3): 1387-1398, doi:10.1109/36.843033.

Martin S, Drucker R, Kwok R, et al. 2004. Estimation of the thin ice thickness and heat flux for the Chukchi Sea Alaskan coast polynya from Special Sensor Microwave/Imager data, 1990–2001. J Geophys Res Oceans, 109(C10): 2004JC002428, doi:10.1029/2004JC002428.

Maykut G A. 1978. Energy exchange over young sea ice in the central Arctic. J Geophys Res Oceans, 83(C7): 3646-3658, doi:10.1029/JC083iC07p03646.

Mecklenburg S, Drusch M, Kerr Y H, et al. 2012. ESA's soil moisture and ocean salinity mission: mission performance and operations. IEEE Trans Geosci Remote Sens, 50(5): 1354-1366, doi:10.1109/TGRS.2012.2187666.

Menashi J D, St Germain K M, Swift C T, et al. 1993. Low-frequency passive-microwave observations of sea ice in the Weddell Sea. J Geophys Res, 98(C12): 22569-22577, doi:10.1029/93jc02058.

Munoz-Martin J F, Rodriguez-Alvarez N, Bosch-Lluis X, et al. 2025. Integrated retrieval of sea-ice salinity, density, and thickness using polarimetric GNSS-R. Remote Sens Environ, 318: 114617, doi:10.1016/j.rse.2025.114617.

Naoki K, Ukita J, Nishio F, et al. 2008. Thin sea ice thickness as inferred from passive microwave and in situ observations. J Geophys Res, 113(C2): 2007JC004270, doi:10.1029/2007jc004270.

Nihashi S, Ohshima K I, Tamura T, et al. 2009. Thickness and production of sea ice in the Okhotsk Sea coastal polynyas from AMSR-E. J Geophys Res, 114(C10): 2008JC005222, doi:10.1029/2008jc005222.

Paţilea C, Heygster G, Huntemann M, et al. 2019. Combined SMAP–SMOS thin sea ice thickness retrieval. Cryosphere, 13(2): 675-691, doi:10.5194/tc-13-675-2019.

Pinori S, Crapolicchio R, Mecklenburg S. 2008. Preparing the ESA-SMOS (soil moisture and ocean salinity) mission–overview of the user data products and data distribution strategy. 2008 Microwave Radiometry and Remote Sensing of the Environment, March 11–14, 2008, Florence: IEEE, 1-4, doi:10.1109/MICRAD.2008.4579480.

Ricker R, Hendricks S, Kaleschke L, et al. 2017. A weekly Arctic sea-ice thickness data record from merged CryoSat-2 and SMOS satellite data. Cryosphere, 11(4): 1607-1623, doi:10.5194/tc-11-1607-2017.

Singh R K, Oza S R, Vyas N K, et al. 2011. Estimation of thin ice thickness from the advanced microwave scanning radiometer-EOS for coastal polynyas in the Chukchi and Beaufort Seas. IEEE Trans Geosci Remote Sens, 49(8): 2993-2998, doi:10.1109/TGRS.2011.2123101.

Tamura T, Ohshima K I. 2011. Mapping of sea ice production in the Arctic coastal polynyas. J Geophys Res, 116(C7): 2010JC006586, doi:10.1029/2010jc006586.

Tamura T, Ohshima K I, Markus T, et al. 2007. Estimation of thin ice thickness and detection of fast ice from SSM/I data in the Antarctic Ocean. J Atmos Ocean Technol, 24(10): 1757-1772, doi:10.1175/jtech2113.1.

Tian-Kunze X, Kaleschke L, Maaß N, et al. 2014. SMOS-derived thin sea ice thickness: algorithm baseline, product specifications and initial verification. Cryosphere, 8(3): 997-1018, doi:10.5194/tc-8-997-2014.

Vant M R, Ramseier R O, Makios V. 1978. The complex-dielectric constant of sea ice at frequencies in the range 0.1–40 GHz. J Appl Phys, 49(3): 1264-1280, doi:10.1063/1.325018.

Xie Y J, Yan Q Y. 2024. Stand-alone retrieval of sea ice thickness from FY-3E GNOS-R data. IEEE Geosci Remote Sens Lett, 21: 2000305, doi:10.1109/LGRS.2024.3352831.

Yu Y, Rothrock D A. 1996. Thin ice thickness from satellite thermal imagery. J Geophys Res Oceans, 101(C11): 25753-25766, doi:10.1029/96JC02242.